THE JOURNAL OF PHYSICAL CHEMISTRY A

Article

pubs.acs.org/JPCA

Imaging and Scattering Studies of the Unimolecular Dissociation of the $BrCH_2CH_2O$ Radical from $BrCH_2CH_2ONO$ Photolysis at 351 nm

Lei Wang,[†] Chow-Shing Lam,[†] Rabi Chhantyal-Pun,[‡] Matthew D. Brynteson,[†] Laurie J. Butler,*[,†] and Terry A. Miller[‡]

[†]The James Franck Institute and Department of Chemistry, The University of Chicago, Chicago, Illinois 60637 United States and [‡]Department of Chemistry, The Ohio State University, Columbus, Ohio 43210 United States

Supporting Information

ABSTRACT: We report a study of the unimolecular dissociation of $BrCH_2CH_2O$ radicals produced from the photodissociation of $BrCH_2CH_2ONO$ at 351/355 nm. Using both a crossed laser-molecular beam scattering apparatus with electron bombardment detection and a velocity map imaging apparatus with tunable VUV photoionization detection, we investigate the initial photodissociation channels of the $BrCH_2CH_2ONO$ precursor and the subsequent dissociation of the vibrationally excited $BrCH_2CH_2O$ radicals. The only photodissociation channel of the precursor we detected upon photodissociation at 351 nm was O−NO bond fission. C−Br photofission and HBr photoelimination do not compete significantly with O−NO photofission at this excitation wavelength. The measured O−NO photofission recoil kinetic energy distribution peaks near 14 kcal/mol and extends from 5 to 24 kcal/mol. There is also a small signal from lower kinetic energy NO product (it would be 6% of the total if it were also from O−NO photofission). We use the O−NO photofission $P(E_T)$ peaking near 14 kcal/mol to help characterize the internal energy distribution in the nascent ground electronic state $BrCH_2CH_2O$ radicals. At 351 nm, some but not all of the $BrCH_2CH_2O$ radicals are formed with enough internal energy to unimolecularly dissociate to $CH_2Br + H_2CO$. Although the signal at $m/e = 93$ (CH_2Br^+) obtained with electron bombardment detection includes signal both from the CH_2Br product and from dissociative ionization of the energetically stable $BrCH_2CH_2O$ radicals, we were able to isolate the signal from CH_2Br product alone using tunable VUV photoionization detection at 8.78 eV. We also sought to investigate the source of vinoxy radicals detected in spectroscopic experiments by Miller and co-workers (*J. Phys. Chem. A* **2012**, *116*, 12032) from the photodissociation of $BrCH_2CH_2ONO$ at 351 nm. Using velocity map imaging and photodissociating the precursor at 355 nm, we detected a tiny signal at $m/e = 43$ and a larger signal at $m/e = 15$ that we tentatively assign to vinoxy. An underlying signal in the time-of-flight spectra at $m/e = 29$ and $m/e = 42$, the two strongest peaks in the literature electron bombardment mass spectrum of vinoxy, is also apparent. Comparison of those signal strengths with the signal at HBr^+, however, shows that the vinoxy product does not have HBr as a cofragment, so the prior suggestion by Miller and co-workers that the vinoxy might result from a roaming mechanism is contraindicated.

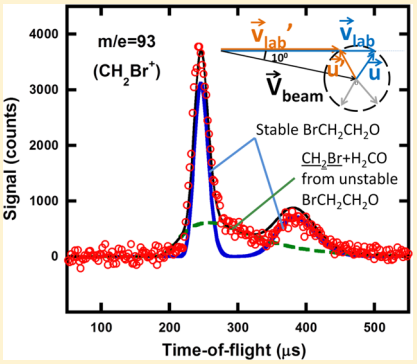

I. INTRODUCTION

The importance of nitrogen oxides in atmospheric chemistry is well-known. As an atmospheric source of NO, alkyl nitrites (RONO, where R represents an alkyl moiety) play a role in mediating atmospheric ozone levels and influence photochemical smog.[1] Interest in characterizing these important phenomena has led to studies on nitrous acid (HONO),[2−5] methyl nitrite (CH_3ONO),[6−10] and *tert*-butyl nitrite ($(CH_3)_3CONO$)[11−14] previously. Here, we focus on the primary photodissociation pathways of a halogenated nitrite at 351 nm, $BrCH_2CH_2ONO$. Miller and co-workers have recently spectroscopically identified several products from the photodissociation of a series of halogenated species XCH_2CH_2ONO (X = F, Cl, Br, OH) at 351 nm.[15] This study aims to characterize the primary photodissociation channels of $BrCH_2CH_2ONO$ and the subsequent unimolecular decomposition of the nascent $BrCH_2CH_2O$ radical formed.

Several studies have focused on characterizing the photodissociation of alkyl nitrites near 351 nm. As a prototype, methyl nitrite photodissociation has been studied both theoretically and experimentally.[6−10] The absorption spectrum in the 351 nm region is assigned to the $S_0 \rightarrow S_1$ transition corresponding to the excitation of a lone pair electron of oxygen to the π^*(NO) antibonding orbital. The potential energy surface of the S_1 state has a shallow minimum above the ground state equilibrium geometry; it results in an indirect vibrational predissociation process.[16] The excited state lifetime is longer than the NO vibrational period. The absorption band shows a progression in the NO stretching mode, and upon O−NO photofission the NO product retains much of this vibrational energy. The S_1 state lifetime of 125 fs reported by

Received: September 25, 2013
Revised: November 21, 2013
Published: January 6, 2014

Mestdagh and co-workers[17] confirms the indirect character of the dissociation process upon photoexcitation to S_1. The photodissociation of other alkyl nitrites in this absorption band, such as CH_3CH_2ONO and $(CH_3)_3CONO$,[18,19] evidence similar predissociation dynamics.

The photodissociation products from halogenated alkyl nitrites may be quite different from those of the well-studied alkyl nitrites described above. The C−Br bond in the $BrCH_2CH_2ONO$ might be cleaved photolytically upon 193 nm excitation, and even at 351 nm one should investigate whether HBr photoelimination competes with primary O−NO photofission. The primary O−NO photofission channel also affords the opportunity to study the subsequent unimolecular dissociation of highly vibrationally excited β-bromoethoxy radicals. (Only the α-bromoethoxy radical has been studied previously, and only computationally.) The present work first determines the internal energy distribution of $BrCH_2CH_2O$ radicals formed from the $BrCH_2CH_2ONO$ precursor photodissociation at 351 nm; then it characterizes the subsequent dissociation of the radical to CH_2Br and H_2CO. We also investigate the source of the vinoxy product reported by Miller and co-workers.

II. METHODS

A. Preparation of Bromoethyl nitrite ($BrCH_2CH_2ONO$). Bromoethyl nitrite ($BrCH_2CH_2ONO$) was synthesized as follows. 2-Bromoethanol ($BrCH_2CH_2OH$, 95%) and sodium nitrite ($NaNO_2$, >99%) were purchased from Sigma Aldrich. Sodium nitrite ($NaNO_2$, 0.4 mol) and deionized H_2O (100 mL) were mixed in a 500 mL round-bottom flask equipped with a stir bar and a 125 mL addition funnel with a Teflon stopcock. The round-bottom flask was placed in an ice bath to cool the mixture to 0 °C, which was maintained for the whole reaction time. 2-Bromoethanol ($BrCH_2CH_2OH$, 0.4 mol), concentrated H_2SO_4 (0.2 mol) and deionized H_2O (7 mL) were mixed together in the addition funnel. This mixture was added to the round-bottom flask dropwise over 20 min with the stirrer set at a medium frequency. The final product mixture was then transferred into a 125 mL separatory funnel. The product mixture separates into a greenish yellow organic layer and nearly transparent aqueous layer. The organic layer, which is mostly $BrCH_2CH_2ONO$, was separated from the aqueous layer and stored at −80 °C to be used within two weeks.

B. Crossed Laser-Molecular Beam Scattering Apparatus. We use a crossed laser-molecular beam scattering apparatus to characterize the recoil kinetic energy and angular distributions of the products upon photodissociation at 351 nm, as well as the products from the secondary unimolecular dissociation of the vibrationally excited $BrCH_2CH_2O$ radicals formed from the initial photodissociation. Introduced from a −18 °C bath, the $BrCH_2CH_2ONO$ molecular beam, seeded in helium gas to a total pressure of 370 Torr, passes through a continuous nozzle heated to 40 °C. The beam then passes through two skimmers en route to the main chamber, where it intersects the 351 nm pulsed laser light softly focused to a ∼6 mm^2 cross-sectional area. The 351 nm light is produced by the XeF transition of an unpolarized Lumonics PM-848 excimer laser and the energy at the crossing volume with the molecular beam is 62.4 mJ/pulse. The laser light propagates along the axis, which is perpendicular to the plane defined by the molecular beam and detector axis, so the light is unpolarized in the scattering plane. The molecular beam can be rotated to different source angles. Here we use a source angle of 10° to allow efficient detection of neutral photofragments, including those with low recoil speeds.

After photodissociation in the interaction region where the laser crosses the molecular beam in our main chamber (with background of $\sim10^{-6}$ Torr), the photofragments can scatter with the velocities determined by the molecular beam velocity and recoil velocity imparted during the photodissociation. If a radical product dissociates within the 2 μs transit time of the interaction region, the products detected also reflect the additional velocity imparted in that dissociation. The products with a resultant velocity vector along the detector axis can be ionized by 200 eV electron bombardment ionization, and then mass-to-charge selected by a quadruple mass spectrometer and detected by a Daly detector. The signal, proportional to the number of ions that strike the Daly detector as a function of time, is counted by a multichannel scaler and accumulated in 2 μs channels. The ion flight time from the ionizer to the detector is calculated using the apparatus ion flight constant of 4.5 μs $amu^{-1/2}$ multiplied by the square root of the detected ion mass. Upon subtracting this ion flight time from the total fight time, we can determine the neutral flight time (given on the horizontal axis in the data plotted herein) for each photofragment or unimolecular dissociation product of the $BrCH_2CH_2O$ radicals. To characterize the parent beam, we rotate the source angle to 0° and raise the chopper wheel operating at 200 Hz.

In this project, we looked for signal at m/e = 30 (NO^+ and H_2CO^+), m/e = 42 (CH_2CO^+), m/e = 82 ($H^{81}Br^+$), m/e = 79 ($^{79}Br^+$), m/e=29 (HCO^+), and m/e = 93 ($CH_2{}^{79}Br^+$). At m/e = 123, little or no signal appeared after 5×10^6 laser shots.

To measure the angular distribution of the NO fragments, we separate the unpolarized 351 nm laser beam into two linearly polarized laser beams with a single-crystal quartz birefringent Pellin-Broca prism. The selected horizontally polarized laser beam is passed through a half-wave plate to rotate the direction of polarization and then intersects the molecular beam in a ∼3.2 mm^2 cross-sectional area. Viewing along the laser propagation axis from the excimer to the main chamber, the principal axis of half-wave retarder is 45° clockwise from the horizontal axis in the half-wave retarder plane, so the horizontally polarized light is rotated to vertically polarized light after passing the half-wave retarder. In this project, data are taken at m/e = 30 for seven polarization angles 0°, 15°, 50°, 90°, 120°, 150°, 180°; each angle is counterclockwise from the vertical axis in the half-wave retarder plane. The data are taken with 3.8×10^6 shots for each angle, split into seven sets to average out any drifts in molecular beam intensity and laser pulse energy.

C. Velocity Map Imaging Apparatus. Additional key data were collected on a velocity map imaging apparatus in this study. The apparatus is described in detail elsewhere,[20−22] so only a brief description will be given here. A beam of 2-bromoethyl nitrite is created by seeding the equilibrium vapor pressure of the liquid sample maintained at −15 °C in helium to a total pressure of 400 Torr. The beam is supersonically expanded through a pulsed valve and passed through a skimmer that collimates the beam. The molecules are then photodissociated using vertically polarized 355 nm light from a Continuum Surelite I-20 Nd:YAG laser. This laser is focused to a ∼1 mm^2 spot and the pulse energies are typically ∼1 mJ. Approximately 40 ns after photodissociation, the molecules are ionized by light tuned to ionize the product of interest (8.78 eV for CH_2Br and 9.08 eV for NO) but not dissociatively ionize other species that might give a signal at the same mass to

dx.doi.org/10.1021/jp4095886 | J. Phys. Chem. A 2014, 118, 404−416

charge ratio. We also used 10.6 eV for the dissociative ionization of vinoxy to m/e = 15 and 10.55 eV to detect a very small signal from vinoxy at the parent m/e = 43). The tunable VUV photoionization light was generated by a resonance enhanced four-wave difference-frequency mixing ($\omega_{VUV} = 2\omega_1 - \omega_2$) scheme in a Kr gas cell (10−15 Torr), where ω_1 and ω_2 represent the fixed ultraviolet (UV) and tunable visible laser frequencies.[23] In this scheme, the UV and visible laser light pulses are respectively generated by two dye lasers (Lambda Physik, FL3002) which are pumped by a common injection-seeded Nd:YAG laser (Continuum Powerlite Precision 9020). The fixed UV frequency ω_1 at 47 046.43 or 49 427.53 cm^{-1} (212.56 or 202.32 nm) is obtained by the third harmonic generation of the laser output at 15 682.14 or 16 475.84 cm^{-1} (637.67 or 606.95 nm) to match the two-photon resonance of the Kr transition, 5p ← 4p at 94 092.86 cm^{-1} or 5p′ ← 4p at 98 855.06 cm^{-1} ($2\omega_1$). The visible frequency ω_2 is generated by the second dye laser, which is tunable to give the desired VUV wavelengths. The resultant ω_{VUV} utilized as the photoionization source is selected by an off-center MgF_2 lens before entering the photoionization region.

The ions pass through an electrostatic lens assembly, which includes a repeller plate and an extractor plate held in a voltage ratio of 1.4:1. The lens assembly accelerates the spherically expanding cloud of ions down the grounded flight tube toward the detector. The detector consists of a position sensitive Chevron microchannel plate (MCP) that is gated by applying a −750 V pulse that coincides with the arrival time of the mass of interest. The ion colliding with the MCP creates an electron cascade, which induces fluorescence on a phosphor screen directly behind the MCP. A CCD camera records the resulting images of the phosphor screen.

D. Computational Method. We calculated the O−NO bond energy in $BrCH_2CH_2ONO$ and optimized the geometries of certain minima and transition states on the $BrCH_2CH_2O$ potential energy surface to calculate the barrier energies at the G4//B3LYP/6-311++G(3df,2p) level of theory. To predict the competition between three possible dissociation channels of the $BrCH_2CH_2O$ radical, we carried out a rough simulation using the MULTIWELL program suite.[24]

III. RESULTS AND ANALYSIS

A. O−NO Bond Photofission in the $BrCH_2CH_2ONO$ Precursor. Figure 1 shows the time-of-flight (TOF) spectrum taken at m/e = 30 (NO^+, H_2CO^+) at a source angle of 10°. The high kinetic energy signal in the spectrum, peaking at arrival times near 130 μs, is the NO photoproduct from primary O−NO bond fission of the precursor, $BrCH_2CH_2ONO$, forming vibrationally hot ground state $BrCH_2CH_2O$ radicals + NO:

$$BrCH_2CH_2ONO + h\nu \rightarrow BrCH_2CH_2O + NO \quad (1)$$

We use forward convolution fitting of the fast peak, shown by the blue solid line, to derive the O−NO bond fission recoil kinetic energy distribution, $P(E_T)$, shown by the blue solid line in Figure 2, peaking near 14 kcal/mol in relative kinetic energy. The photofragment angular distribution measured for this signal is given in the Supporting Information. It is very anisotropic and so indicates that the O−NO bond fission is prompt with respect to molecular rotation and the electronic transition momentum is perpendicular to the recoil velocity vector. There is also a broad signal at longer flight times that peaks near 240 μs in the m/e = 30 spectrum. We do not know the source of this NO signal. It is possible that the precursor photodissociates to NO + $BrCH_2CH_2O$ via an alternative channel with lower kinetic energy release (KER). A bimodal

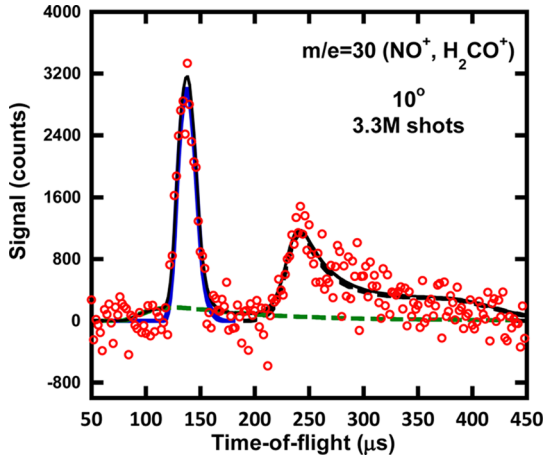

Figure 1. Time-of-flight spectrum of the signal at m/e = 30 (NO^+, H_2CO^+). The data are shown in open circles, and the overall fit is the sum of three contributions. The two contributions to the signal from NO include both a narrow component extending from 110 to 180 μs, assigned to O−NO photofission (eq 1) and shown as a blue line, and a slower component extending from 210 to 350 μs, shown as a dashed black line. The distribution of recoil kinetic energies, $P(E_T)$, for O−NO bond photofission (351 nm excitation) derived from the forward convolution fitting of these data is shown in Figure 2; we assign the dominant fast component to O−NO photofission. The source of the low kinetic energy minor NO signal shown as the dashed black line is uncertain (we only fit it to O−NO photofission to display its relative probability in Figure 2). Because some of the momentum matched $BrCH_2CH_2O$ radicals formed in O−NO photofission have enough internal energy to dissociate to CH_2Br + H_2CO, the H_2CO can also give a signal at m/e = 30 (H_2CO^+). We show formaldehyde's contribution to the m/e = 30 TOF as a dashed green line. The recoil kinetic energy distribution for that channel is derived using imaging data for CH_2Br in section IIID and accounting for a multiphoton contribution to the imaging data.

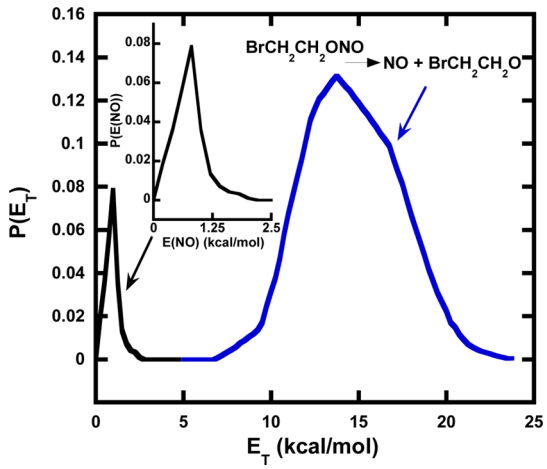

Figure 2. Total recoil kinetic energy distribution, $P(E_T)$, of the NO and $BrCH_2CH_2O$ resulting from O−N bond fission in the photodissociation of $BrCH_2CH_2ONO$ at 351 nm. The $P(E_T)$ shown as the blue solid line, peaking near 14 kcal/mol, is derived from the forward convolution fitting of the fast peak in the m/e = 30 (NO^+) signal in Figure 1. The NO signal fit by the minor low kinetic energy distribution peaking near 1 kcal/mol (black line) may not have $BrCH_2CH_2O$ as a cofragment, so we show its individual ($E_{T,NO}$) kinetic energy distribution in the inset.

dx.doi.org/10.1021/jp4095886 | J. Phys. Chem. A 2014, 118, 404−416

kinetic energy distribution for R−X photofission is often observed when one channel produces electronically excited radicals. However, in this case there is no excited state of the $BrCH_2CH_2O$ product that is an obvious candidate (the A state is far too low in energy and the B state is too high). In addition, in the Supporting Information we show velocity map images that reveal an opposite sign for the anisotropy parameters for the low kinetic energy NO photoproduct. Thus we think it is unlikely that this NO product is from O−NO photofission in the $BrCH_2CH_2ONO$ precursor. Nevertheless, to show it is a minor component we tried to fit it to a $P(E_T)$ assuming it is NO recoiling from $BrCH_2CH_2O$. Then the forward-convolution fit shown as the dashed black line in Figure 1 gives the low kinetic energy $P(E_T)$ peaking near 1 kcal/mol in Figure 2. The integrated areas of the major O−NO fission $P(E_T)$ in blue to the $P(E_T)$ that fit this low kinetic energy NO signal is 94:6, so the slower NO is a minor photoproduct, potentially from an impurity in the synthesized sample. Because we cannot be certain that $BrCH_2CH_2ONO$ is the photolytic precursor for this NO signal, we give in the inset in Figure 2 the kinetic energy distribution of the NO alone (not the total kinetic energy of both fragments) that gives the dashed black line fit in Figure 1.

Because formaldehyde, one of the products observed in Miller et al.'s spectroscopic studies, can also give signal at m/e = 30 upon electron bombardment ionization, we also detected the NO product using single-photon VUV ionization at 9.08 eV and other nearby photon energies in our imaging apparatus. In the imaging experiments we photodissociated $BrCH_2CH_2ONO$ with 355 nm photons from the third harmonic of a Nd:YAG laser rather than 351 nm light. We show those images and the $P(E_T)$'s derived from them in the Supporting Information. The images taken with 9.08 eV and higher photoionization energies and a photodissociation wavelength of 355 nm rather than 351 nm show a major component similar to that of the $P(E_T)$ in the blue line in Figure 2 peaking near 14 kcal/mol, but shifted to slightly lower recoil kinetic energies (by about 1 kcal/mol) due to the lower photodissociation photon energy. (We are able to detect all the NO product with a photoionization laser tuned to a bit lower energies than the adiabatic IE of 9.26 eV because the NO product is expected to be formed with 1, 2, or 3 quanta in vibration, but not with 0 quanta in vibration. This is detailed in the next section.) The images also evidence some lower kinetic energy NO products, supporting the assignment of the slower feature in Figure 1 to NO rather than to formaldehyde. The momentum-matched $BrCH_2CH_2O$ radicals formed in the higher recoil kinetic energy channel were also detected with 200 eV electron bombardment ionization. Before presenting that data, we first present some calculated energetics and an estimate of the internal energy distribution of these radicals. The majority of them are formed with enough internal energy to dissociate to $CH_2Br + H_2CO$; evidence of that product channel is given in section IIID. The fit to the resulting H_2CO signal at m/e = 30 is shown as the green dashed line in Figure 1.

B. Estimating the Internal Energy in the $BrCH_2CH_2O$ Radicals. Much of our study focuses on the unimolecular dissociation of the momentum-matched $BrCH_2CH_2O$ radicals formed from photofission of the O−NO bond, so the distribution of internal energies in those nascent radicals are of interest. Our theoretical calculations on the $BrCH_2CH_2O$ potential energy surface at G4//B3LYP/6-311++G(3df,2p) level of theory give the energetics of the zero-point corrected minima and transition states shown in Figure 3. The product

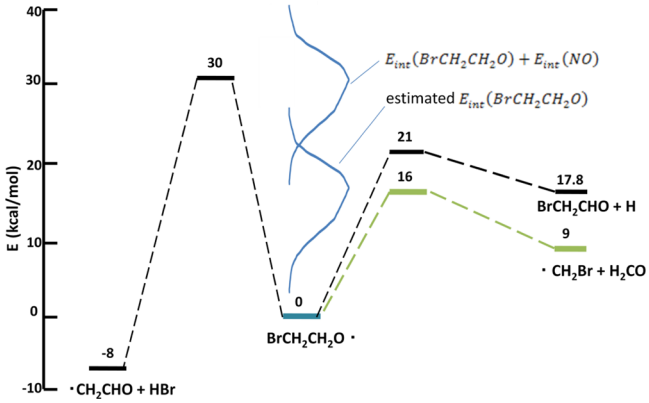

Figure 3. Internal energy distribution for nascent ground state $BrCH_2CH_2O$ radicals formed in the photodissociation for $BrCH_2CH_2ONO$ at 351 nm. This distribution is superimposed on the critical points on the potential energy surface calculated at the G3//B3LYP/6-311++G (3df,2p) level of theory. The upper curve, labeled $E_{int}(BrCH_2CH_2O) + E_{int}(NO)$, is derived directly, using eq 2 in the text, from the major component of the O−NO photofission $P(E_T)$ peaking near E_T = 14 kcal/mol shown in blue in Figure 2. The lower curve, which subtracts off the estimated average internal energy of 14 kcal/mol in the NO cofragment, peaks near an internal energy of 16 kcal/mol in the nascent $BrCH_2CH_2O$ radicals. See the text for details.

channel with by far the lowest barrier is that leading to $CH_2Br + H_2CO$, so as expected our simulation using the MULTIWELL program suite and these calculated transition states suggests that the $CH_2Br + H_2CO$ channel would dominate the product branching of our vibrationally excited ground state $BrCH_2CH_2O$.

Because much of the available energy upon photodissociation was partitioned into the relative kinetic energy of the recoiling NO and $BrCH_2CH_2O$ radicals and the internal energy of the NO cofragment, the internal energy of the momentum-matched $BrCH_2CH_2O$ radicals is largely below 30 kcal/mol. In Figure 3, we show our estimate of the internal energy distribution of the nascent ground electronic state $BrCH_2CH_2O$ radicals (with details to follow in this section) superimposed on a plot of the energetic barriers the radical must surmount to undergo subsequent dissociation. Some of the $BrCH_2CH_2O$ radicals are formed with internal energy below the predicted dissociation barrier to $CH_2Br + H_2CO$, so those radicals are stable to secondary dissociation. Others have enough internal energy to undergo subsequent dissociation. Two internal energy curves are shown in Figure 3. The upper one shows the total internal energy in both the NO and the momentum-matched $BrCH_2CH_2O$ radicals; this is derived directly from our data. The lower curve in Figure 3 is an estimate of the internal energy distribution of the $BrCH_2CH_2O$ radicals exclusively. We estimate the average rovibrational energy of the NO cofragment to be 14 kcal/mol and subtract it from the total internal energy distribution as described in the next few paragraphs. (This way of estimating the internal energy distribution of $BrCH_2CH_2O$ is rough, as it neglects the fact that there is a distribution of internal energies in the NO cofragment.)

We first use our measured O−NO bond fission recoil kinetic energy, E_T, distribution in blue line in Figure 2 to directly derive the internal energy distribution in the pair of nascent radicals (NO and CH_2CH_2BrO) using conservation of energy:

dx.doi.org/10.1021/jp4095886 | J. Phys. Chem. A 2014, 118, 404−416

$$E_{int}(BrCH_2CH_2O) + E_{int}(NO) = h\nu + E_{BrCH_2CH_2ONO} - D_0(O-NO) - E_T \quad (2)$$

The result is depicted in the upper curve in Figure 3. In eq 2, the 351 nm photon energy, $h\nu$, is 81.5 kcal/mol; the dissociation energy of the O−NO bond, D_0(O−NO), is 39.0 kcal/mol, calculated at the G4//B3LYP/6-311++G(3df,2p) level of theory. $E_{BrCH_2CH_2ONO}$ is the internal energy of the $BrCH_2CH_2ONO$ precursor; we assume the rotational energy of the precursor is effectively cooled in the supersonic expansion and the vibrational energy can be estimated by a thermal distribution, with an average of 2.84 kcal/mol, at the nozzle temperature of 40 °C. The resulting internal energy distribution in the pair of products is shown in the top curve in Figure 3, derived from the measured $P(E_T)$ in blue line in Figure 2.

Though our measured $P(E_T)$ allows us to directly determine the internal energy distribution in the pair of products, NO and $BrCH_2CH_2O$, one would of course prefer to know the internal energy distribution of the $BrCH_2CH_2O$ radicals alone. The NO carries away a significant amount of energy in vibration and rotation. We describe below how we estimate this on average to be about 14 kcal/mol, so in Figure 3 we show a lower estimated distribution of internal energies for the $BrCH_2CH_2O$ radical alone. The actual distribution of internal energy in the nascent $BrCH_2CH_2O$ radicals would be somewhat broader than that shown in Figure 3 because the NO cofragment has a distribution of internal energies about this average.

To estimate the average amount of vibrational energy in the NO cofragment, we note that the UV absorption spectrum of $BrCH_2CH_2ONO$, shown in the Supporting Information, is quite similar to, but slightly shifted in energy from, that of other alkyl nitrites. The UV absorption spectrum of CH_3ONO between 300 and 380 nm evidences a vibrational progression in the N═O stretch.[25] This normal mode in S_1 is anharmonic so the energetic difference between the adjacent levels decreases from 1142 to 926 cm^{-1}. The N═O stretching mode is 1625 cm^{-1} in the ground electronic state; the vibrational wavenumber is reduced to 1142 cm^{-1} in S_1. Benoist D'Azy et al.[10] reported a state selective photodissociation experiment in which they tuned the excitation energy to features in the absorption spectrum corresponding to successively higher vibrational quanta in this mode in S_1 and measured the vibrational state distribution of the NO product. (That paper labels the features in the absorption spectrum of methyl nitrite as 3_0^1, 3_0^2, etc. despite the fact that the mode is not v_3.) When they excite S_1 at an energy that deposits 1 quantum in the NO stretch in S_1, the NO product is observed to have a 75% population in v″ = 0 and 25% population in v″ = 1. When CH_3ONO is excited at 350 nm, the state with 2 quanta of vibration in the NO stretch in S_1 is excited and the NO product has a vibrational quantum state distribution that peaks at v″ = 1 (50%) with a lower population in v″ = 0 (20%) and substantial population in v″ = 2 (30%). The UV absorption spectrum of $BrCH_2CH_2ONO$ shows a nearly identical vibrational progression, but shifted by about 15 nm to the red, so exciting $BrCH_2CH_2ONO$ with our 351 nm laser excited the NO in the O—NO moiety to a higher vibrational level, with three quanta in the NO stretch, than 351 would have in CH_3ONO. Thus, we estimate the energy in vibration for our NO product using the vibrational distribution measured by Benoist D'Azy et al. for dissociation of CH_3ONO with 3 quanta in the NO stretch in S_1 (the band at 338 nm); the average vibrational energy they measure in the NO product is ~3400 cm^{-1} and there is no NO formed in v″ = 0. Our data in the Supporting Information, Figure S3, support the conclusion that no NO is formed in v″ = 0; detecting NO with photoionization at 9.08, 9.28, and 9.58 eV gives identical velocity distributions for the $P(E_T)$ peaking near 14 kcal/mol. We also can estimate the rotational energy of the NO product using prior results on CH_3ONO. Although the total recoil kinetic energy is different in CH_3ONO than in $BrCH_2CH_2ONO$, the speed of the NO in the center of mass frame is very similar, about 1800 cm^{-1} at the peak of the $P(E_T)$. Given this, we expect the energy partitioned to rotation of the NO would be almost the same as for CH_3ONO photofission upon excitation in the analogous absorption feature. Thus we estimate the $\langle E_{rot} \rangle$ of NO to be about 1500 cm^{-1} on the basis of weighting the rotational energies for each of the NO vibrational quantum states reported by Benoist D'Azy et al. (From their study, we anticipate higher relative population of v″ = 0 when 355 nm is used in place of 351 nm in excitation. This is important as our imaging data were taken with 355 nm excitation, not 351 nm. In the Supporting Information, the images obtained at photon energies higher than 9.28 eV, which are above the adiabatic IE of vibrational ground state of NO, show an extra component of intermediate recoil kinetic energy, which could not be used to fit the scattering data. We ascribe this part to the additional NO with v″ = 0 produced upon excitation at 355 nm.)

To summarize, Figure 3 shows in the lower curve our estimate of the internal energy distribution of the $BrCH_2CH_2O$ radicals alone, assuming the partitioning of vibrational and rotational energy to the NO cofragment is the same as that of alkyl nitrite excited in the analogous S_1 vibrational feature. The estimated internal energy distribution is superimposed on the calculated barriers to the dissociation of the $BrCH_2CH_2O$ radical. The actual internal energy distribution would be somewhat broader, as we have only accounted for the average internal energy in the NO cofragment, but it is clear that one can expect both stable $BrCH_2CH_2O$ radicals and some that dissociate to $CH_2Br + H_2CO$. This internal energy in $BrCH_2CH_2O$ is partitioned between rotational and vibrational energy, so some of the radicals with a total internal energy above the dissociation barrier may still be stable to subsequent dissociation due to conservation of angular momentum.

C. Detecting the Stable $BrCH_2CH_2O$ Radicals. Because the $BrCH_2CH_2O$ radicals are momentum-matched to the NO coproduct, the speed distribution and TOF spectrum of the $BrCH_2CH_2O$ radicals that do not dissociate can be predicted from the NO detected in the spectrum in Figure 1, the signal fit shown as the blue line between 120 and 180 μs. (If $BrCH_2CH_2O$ is formed in conjunction with the minor low-kinetic-energy NO products detected in Figure 1, they would all have enough energy to dissociate, so would not be detected.) The stable $BrCH_2CH_2O$ radicals did not give a signal at parent ion m/e = 123 or isotopic 125, upon 200 eV electron bombardment ionization, but instead were dissociatively ionized to give signals at m/e = 42, CH_2CO^+ (Figure 4), and m/e = 79, $^{79}Br^+$ (Figure 5), in addition to other daughter ions. The excellent fits in those spectra were derived from the $P(E_T)$ in blue line in Figure 2 peaking near E_T = 14 kcal/mol. In our initial fitting we presupposed that the higher recoil kinetic energies in this distribution would be more likely to generate radicals stable to subsequent dissociation. However, the best fit to the stable radical spectrum in Figure 4 results if the entire $P(E_T)$ peaking near 14 kcal/mol in Figure 2 is used. This

dx.doi.org/10.1021/jp4095886 | J. Phys. Chem. A 2014, 118, 404−416

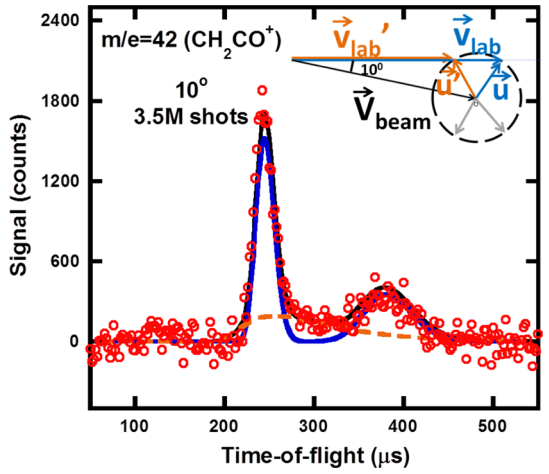

Figure 4. Time-of-flight spectrum of the signal at m/e = 42 (CH_2CO^+). The data are shown in open circles and the whole fit is shown as a black solid line. This spectrum contains the contribution from the dissociatively ionized $BrCH_2CH_2O$ that are stable to secondary dissociation, fit as a blue solid line using the O−NO photofission $P(E_T)$ shown in blue in Figure 2. The fit is bimodal because, as shown by the Newton circle calculated at E_T = 15 kcal/mol in the inset, the magnitude of the recoil velocity $\vec{u}$ imparted to the $BrCH_2CH_2O$ allows backscattered recoil velocities, shown as $\vec{u}'$ in the inset, to give a second slower laboratory velocity, shown as $\vec{v}'_{lab}$, with longer arrival times in the TOF spectrum. The same kinetic energy release also gives the signal peaking near 230 microseconds, as shown by the unprimed vectors in the inset. The NO TOF spectrum in Figure 1 only shows the forward-scattered component from the $P(E_T)$ peaking near 14 kcal/mol because the backward-scattered part of the Newton circle gives a laboratory velocity that is flying away from the detector, not toward it. (If the lower kinetic energy NO product results from O−NO photofission, the $BrCH_2CH_2O$ cofragments, if any survived subsequent dissociation, would not be scattered into our detector at this source angle.) The m/e = 42 spectrum also evidences a broad underlying signal assigned to vinoxy radical. The fit shown by the orange line is generated from a net speed distribution of the vinoxy signal shown in section IIIE, in Figure 12. See the Supporting Information for the $P(E_{T,2°})$ used to assess whether this underlying vinoxy signal might be from the dissociation of 2-bromoethoxy radicals to vinoxy + HBr.

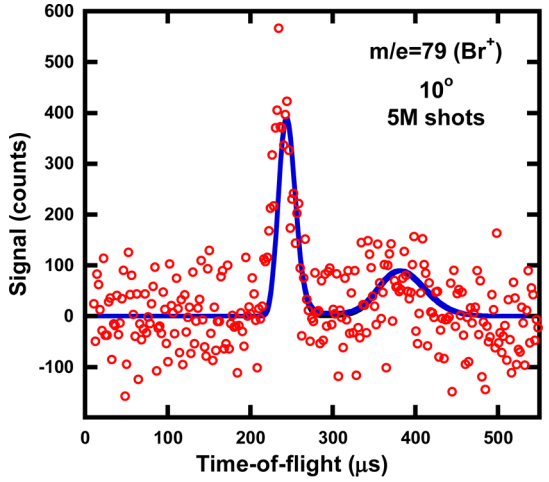

Figure 5. Time-of-flight spectrum of the signal at m/e = 79 (Br^+) resulting from neutral $BrCH_2CH_2O$ photoproducts that dissociatively ionize. The data are shown in open circles, and the fit as a solid blue line is derived from the $P(E_T)$ shown in Figure 2.

indicates that the change in the distribution of internal energies in the NO at each E_T effectively diminishes the expected anticorrelation between E_T and the internal energy in the $BrCH_2CH_2O$ radicals. In looking at the fit in Figure 4, note that the TOF profile of the stable radicals is bimodal for a simple reason, shown in the inset. The signal peaking near 380 microseconds is from $BrCH_2CH_2O$ radicals that have back-scattered velocities in the center-of-mass reference frame (shown with primes in the Newton circle in the inset in Figure 4).

D. CH_2Br + H_2CO from the Dissociation of Vibrationally Excited $BrCH_2CH_2O$ Radicals. The $BrCH_2CH_2O$ formed in the ground electronic state with enough vibrational energy to surmount the 16 kcal/mol barrier shown in green in Figure 3 can dissociate to CH_2Br and H_2CO.

$$BrCH_2CH_2O \rightarrow CH_2Br + H_2CO \quad (3)$$

The TOF spectrum obtained at m/e = 93, $CH_2{}^{79}Br^+$, using electron bombardment ionization is dominated by signal from dissociative ionization of the stable $BrCH_2CH_2O$ radicals shown by the blue fit to the spectrum in Figure 6. However,

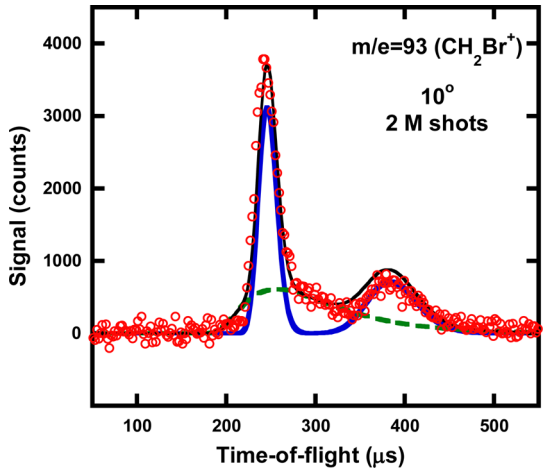

Figure 6. Time-of-flight spectrum of the signal at m/e = 93 (CH_2Br^+). The data are shown in open circles, and the overall fit is shown as a solid black line. This spectrum contains the contribution from the dissociatively ionized $BrCH_2CH_2O$ that are stable to secondary dissociation, fit as a blue solid line using the high kinetic energy portion of the $P(E_T)$ in Figure 2. The spectrum also evidences a contribution from dissociation of $BrCH_2CH_2O$ to CH_2Br + H_2CO; that fit, shown by a green dashed line, was derived from fitting the signal with the vector sum of the velocity imparted to the $BrCH_2CH_2O$ radicals using the $P(E_T)$ peaking near 14 kcal/mol in Figure 2 and the velocity imparted to the CH_2Br product. The $P(E_{T,2°})$ used to calculate the latter velocity is shown in Figure 8; it was derived from fitting the portion of the net speed distribution shown as the green dashed line in Figure 7, measured in the velocity map imaging apparatus. The angular distribution between these vectors was assumed to be isotropic.

a small underlying signal shown by the dashed green line fit in Figure 6 is apparent. To confirm that the broad underlying signal fit as the dashed green line is due to the CH_2Br products from the dissociation of vibrationally excited $BrCH_2CH_2O$ radicals (eq 3), we took a velocity map image at m/e = 93 and tuned the photoionization laser below the appearance energy (AE) of CH_2Br^+ from $BrCH_2CH_2O$ radicals. The calculated IE of $BrCH_2CH_2O$ radicals is 8.7 eV, and the adiabatic appearance energy of CH_2Br^+ from the photoionization of $BrCH_2CH_2O$

dx.doi.org/10.1021/jp4095886 | J. Phys. Chem. A 2014, 118, 404−416

radicals is predicted to be 9.07 eV using the G4//B3LYP/6-311++G(3df,2p) level of theory. Thus to selectively detect the CH_2Br product from eq 3 without contamination from daughter ions of stable radicals, we used tunable VUV photoionization at 8.78 eV; the CH_2Br net speed distribution obtained is shown in Figure 7. (The raw velocity map image is given in the Supporting Information for several VUV photoionization energies between 8.68 and 9.58 eV.) The image includes some high net velocity CH_2Br^+ signal that is presumed to be multiphoton in origin, as it does not appear in the m/e = 93 TOF spectra. Thus Figure 7 shows as a green dashed line the measured net speed distribution of the CH_2Br products from the unimolecular dissociation of $BrCH_2CH_2O$ radicals. (The multiphoton component is shown purple line.) Of course, the net velocity of the CH_2Br products is the vector sum of the velocity of the initial $BrCH_2CH_2O$ radical and the additional velocity imparted to the CH_2Br product when the radical dissociates. Thus to fit this green-dashed contribution shown in Figures 6 and 7, we derive the distribution of energies partitioned to relative kinetic energy when the radical dissociates, $E_{T,2°}$, by forward convolution fitting of the CH_2Br net speed distribution. The resulting $P(E_{T,2°})$ is shown in Figure 8. Details follow.

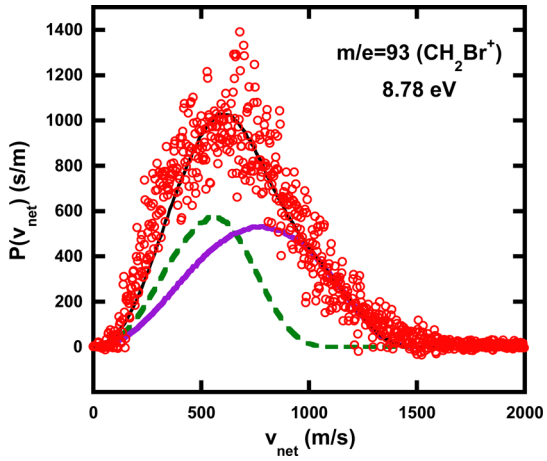

Figure 7. Distribution of net speeds of the CH_2Br fragment from the dissociation of $BrCH_2CH_2O$ radicals. The velocity map image, shown in the Supporting Information, taken at CH_2Br^+ (m/e = 93) includes both single-photon signal and faster velocity signal assumed to be multiphoton in the VUV light. When $BrCH_2CH_2ONO$ absorbs a single 351/355 nm photon, the resulting $BrCH_2CH_2O$ radicals can dissociate to CH_2Br + H_2CO but cannot result in higher velocity CH_2Br detected in the image. The higher velocity component shown in purple must thus result from multiphoton dissociation and ionization by the VUV light. The single-photon component, shown by the green dashed line, is identified by requiring it to have the same velocity distribution as the underlying signal fit shown as the green-dashed line in Figure 6. The multiphoton VUV signal (purple line fit) of course did not contribute to the m/e = 93 TOF spectrum in Figure 6. Thus we identified the multiphoton component by subtracting the single-photon component from the total. Note that the $BrCH_2CH_2O$ radicals were generated from the photodissociation of $BrCH_2CH_2ONO$ at 355 rather than at 351 nm, but the slight difference in initial velocity imparted to the $BrCH_2CH_2O$ radicals, even in this higher recoil kinetic energy portion of the O−NO fission $P(E_T)$, does not substantially influence the $P(E_{T,2°})$ that fits these data. The forward convolution fit to the speed distribution, shown as the green dashed line, allowed us to derive the recoil kinetic energies, $P(E_{T,2°})$, in Figure 8, imparted to the CH_2Br + H_2CO products when $BrCH_2CH_2O$ radicals from the dominant O−NO photofission channel undergo subsequent dissociation.

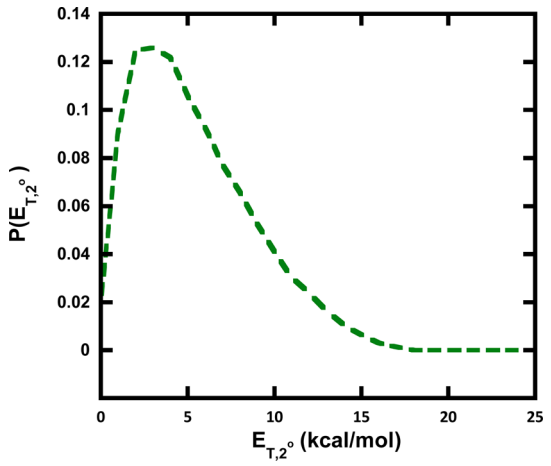

Figure 8. Recoil kinetic energy distribution $P(E_{T,2°})$ for the dissociation of $BrCH_2CH_2O$ radicals to CH_2Br + H_2CO. It was derived from forward-convolution fitting of the net speed distribution shown as the green dashed line in Figure 7 of the CH_2Br fragment detected in our velocity map imaging apparatus. The fit this $P(E_{T,2°})$ gave to our data, using the initial velocity of the dissociating $BrCH_2CH_2O$ radicals calculated from the blue line $P(E_T)$ in Figure, 2 and an isotropic angular distribution between that velocity and the velocity imparted to the CH_2Br product, is shown by the green dashed lines in Figures 6 and 7. The small signal in the m/e = 29 TOF spectrum (Figure 10) from the H_2CO coproduct is also fit with the same primary and secondary $P(E_T)$'s.

To derive the distribution of relative kinetic energies $P(E_{T,2°})$ when the $BrCH_2CH_2O$ radicals dissociate to CH_2Br + H_2CO from our data, we use the O−NO bond fission $P(E_T)$ in blue in Figure 2 to determine the velocity of the radicals that dissociate and then iteratively adjust the distribution of relative kinetic energies $P(E_{T,2°})$ when the $BrCH_2CH_2O$ radicals dissociate to CH_2Br + H_2CO to model the additional velocity imparted to the CH_2Br product. The adequate fit to the measured net speed distribution of CH_2Br shown in dashed green line in Figure 7 was obtained using the $P(E_{T,2°})$ shown in Figure 8 and an isotropic angular distribution between the two velocity vectors. We used the data analysis code developed in our group and described in ref 26. Note that the lowest net speed signal is underfit in Figure 7; this is likely because we have used the entire O−NO photofission $P(E_T)$ (Figure 2, blue line) to calculate the velocity distribution of the radicals that dissociate. It is likely, however, that the highest recoil kinetic energies in the O−NO photofission $P(E_T)$ do not result in radicals that dissociate. Thus the net velocities calculated for the CH_2Br and H_2CO products is artificially high.

To fit the same contribution to the m/e = 93 (CH_2Br^+) TOF spectrum in Figure 6 taken in our crossed laser-beam scattering apparatus, we also used the blue line $P(E_T)$ shown in Figure 2 and the secondary kinetic energy distribution $P(E_{T,2°})$ predicted from fitting the velocity map imaging data shown in green dashed line in Figure 8 with an isotropic $I(\theta)$ for the distributions of angles between the velocity vector of the dissociating radical and the additional velocity imparted to the radical as it dissociates. The predicted fit shown in dashed green line in Figure 6 well accounts for the underlying signal from CH_2Br in this spectrum. The CH_2Br products from the CH_2Br

dx.doi.org/10.1021/jp4095886 | J. Phys. Chem. A 2014, 118, 404−416

+ H_2CO product channel (eq 3) may also undergo dissociative ionization upon electron bombardment ionization and give a small signal at $H^{81}Br^+$ (m/e = 82). This contribution to the m/e = 82 TOF spectrum is shown in dashed green line in Figure 9.

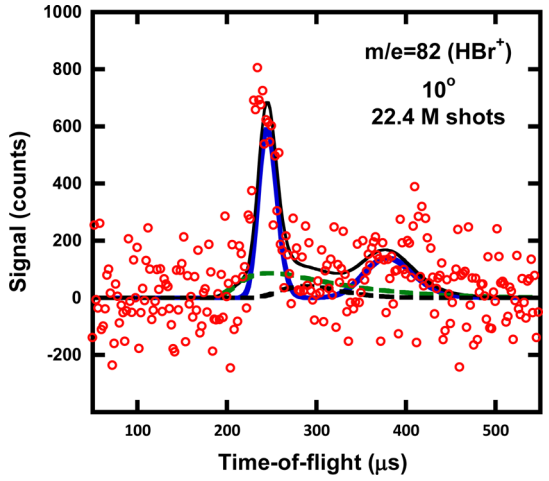

Figure 9. Time-of-flight spectrum of the signal at m/e = 82 ($H^{81}Br^+$). The data are shown in open circles and the overall fit (shown by the solid black line) is potentially the sum of three contributions. The solid blue line shows the contribution from stable $BrCH_2CH_2O$ radicals that dissociatively ionize to HBr^+. The green dashed line shows the predicted arrival times of the CH_2Br radicals if they dissociatively ionize to HBr^+ and the black dashed line shows the predicted arrival times for the HBr product if $BrCH_2CH_2CO$ radicals dissociate to vinoxy + HBr. The signal at HBr^+ would be a factor of 80 stronger if the vinoxy were from this source, so this dashed black line fit is for analysis purposes only (to derive the correction factor in the comparison of signals in section III, eq 6).

Finally, we can also identify signals from the momentum-matched formaldehyde products formed when the $BrCH_2CH_2O$ radicals dissociate to CH_2Br + H_2CO in the m/e = 30 spectrum shown in Figure 1. Although the m/e = 30 TOF spectrum is dominated by signals from NO photofragments, there is a broad underlying signal from formaldehyde that is fit as the green dashed line in Figure 1. This signal is momentum-matched (for the step where the $BrCH_2CH_2O$ radical dissociates) to the CH_2Br signal detected in our imaging experiments and fit as the green dashed line in Figure 7. (Note that the imaging experiments were done with a photodissociation laser at 355 nm whereas the scattering experiments were done at 351 nm, but this makes a negligible difference to the speed distribution of the final dissociation products of the radicals.) Electron bombardment ionization of formaldehyde is well-known to result in substantial signal at both m/e = 30 and m/e = 29, but we only integrated the signal at m/e = 29 for 0.4 million laser shots, so the signal from formaldehyde is barely discernable in Figure 10. The green dashed line fit to the H_2CO product in Figure 1 and the possible contribution in Figure 10 are generated with the same two $P(E_T)$'s (Figures 2 and 8) derived from fitting the CH_2Br speed distribution in Figure 7. The CH_2Br signal fit as the dashed green line in Figure 7 is selectively detected in our imaging apparatus without overlapping contributions from dissociative ionization of other species.

E. Detecting Vinoxy Radical Products. One motivation for conducting this study was to identify the source of the vinoxy radical products that were detected in the spectroscopic

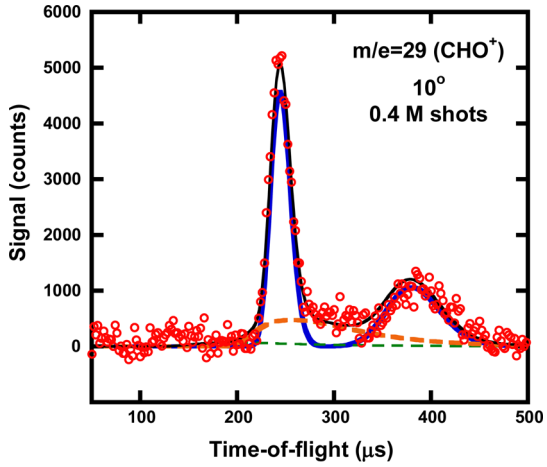

Figure 10. Time-of-flight spectrum of the signal at m/e = 29 (CHO^+). The data are shown as open circles, and the overall fit is shown by the solid black line. The fit shown as the blue solid line shows the contribution from stable $BrCH_2CH_2O$ radicals that dissociatively ionize to CHO^+; the fit is calculated from the high kinetic energy portion of the $P(E_T)$ in Figure 2. Some $BrCH_2CH_2O$ radicals also dissociate to CH_2Br + H_2CO; the H_2CO could give a signal at m/e = 29. This possible contribution is shown by the broad minor underlying fit given as the green dashed line; the fit was derived from the vector sum of the velocity imparted to the $BrCH_2CH_2O$ radicals using the $P(E_T)$ peaking near 14 kcal/mol in Figure 2 and the velocity imparted to the H_2CO product using the $P(E_{T,2°})$ in Figure 8 and an isotropic angular distribution. The underlying signal shown as the orange line is assigned to a contribution to vinoxy in this spectrum; that fit was derived from the net speed distribution shown in Figure 12 and an isotropic angular distribution.

experiments of Miller and co-workers. They tentatively attributed it to the reaction

$$BrCH_2CH_2O \rightarrow HBr + CH_2CHO \quad (4)$$

and suggested that a roaming mechanism might explain why it is able to compete with the much lower barrier CH_2Br + H_2CO product channel. Upon electron bombardment detection, vinoxy is known to undergo dissociative ionization to m/e = 42 and m/e = 29 with high probability.[27,28] There is a broad underlying signal apparent in both our m/e = 42 TOF spectrum in Figure 4 and our m/e = 29 TOF spectrum in Figure 10, though the major signal in both spectra is from the dissociative ionization of the stable $BrCH_2CH_2O$ radicals. (The magnitude of the underlying signal at m/e = 29 is much larger compared to the underlying signal at m/e = 42 than one would expect from the published mass spectrum.) Although we assign this broad underlying contribution shown in orange dashed line in the TOF data at m/e = 42 (Figure 4) and m/e = 29 to vinoxy, we do not believe it is a product from the reaction in eq 4; we explain later in this section. To rid ourselves of the signal from dissociative ionization of stable radicals in the m/e = 42 and 29 spectra, we also sought to detect vinoxy radicals using tunable VUV photoionization detection in our imaging apparatus. Two groups[29,30] report detecting radicals with photoionization detection at m/e = 15, so we looked for signal at both m/e = 43 and m/e = 15 as the cation dissociates to CO + CH_3^+.

The speed distributions of the products detected at m/e = 43 using a photoionization energy of 10.55 eV are shown in Figure 11. The signal is tiny; the spectra were integrated for 150 000 laser shots. The data in the lower frame are taken using a lower intensity of the 10.55 eV photoionization source; comparison

dx.doi.org/10.1021/jp4095886 | J. Phys. Chem. A 2014, 118, 404−416

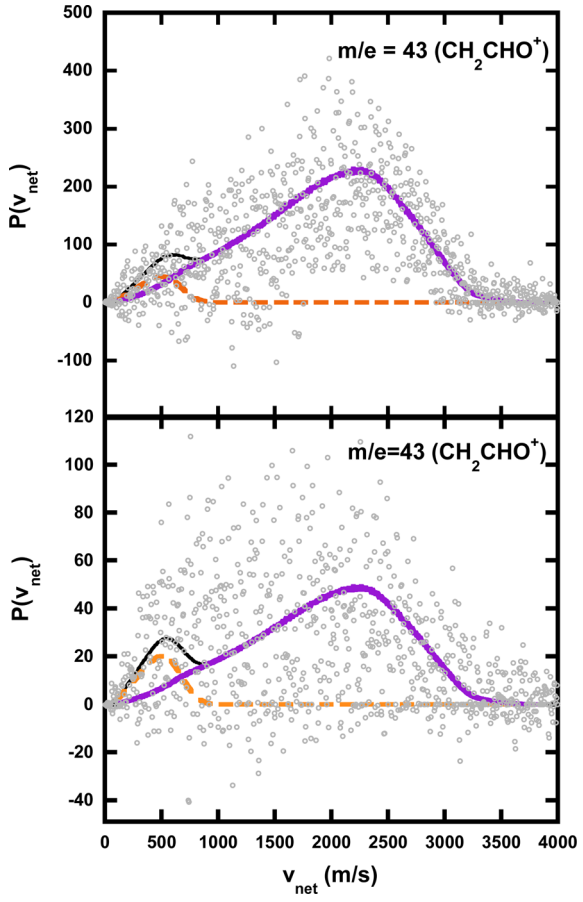

Figure 11. Distribution of net speeds of the signal at m/e = 43 (CH_2CHO^+), derived from the image shown in the Supporting Information, using a photoionization energy of 10.55 eV. The top frame shows the data taken at high VUV laser intensity, and the lower frame shows data taken at low VUV intensity. Clearly, most of the signal extending from 500 to 3500 m/s is from a multiphoton process (Supporting Information). The slower signal fit by the dashed orange line is assigned to vinoxy radicals by also requiring that the speed distribution match the signal fit by the orange dashed line in the m/e = 42 TOF spectrum in Figure 4 (using an isotropic angular distribution). This speed distribution also fits the underlying signal shown as the orange dashed line in the m/e = 29 TOF spectrum in Figure 10. The speed distribution of the orange component alone is given in Figure 12.

with the higher intensity spectrum in the upper frame shows that much of the signal with speeds between 1500 and 3300 m/s is multiphoton in nature. We thus fit the spectra with two components, the high-speed multiphoton signal (purple line), and the more important signal at low speeds peaking near 500 m/s and extending to 800 m/s. The lower portion of the speed distribution, shown by the dashed orange line, may be either fit with a distribution of net speeds imparted to the vinoxy radicals, independent of mechanism, or fit by the net speed distribution assuming the vinoxy arises from the dissociation of $BrCH_2CH_2O$ radicals formed from the minor low kinetic energy component of the O−NO photofission $P(E_T)$ shown in Figure 2. The latter is presented in the Supporting Information, as that allows us to predict the velocity distribution of the momentum-matched HBr if indeed vinoxy is formed from the reaction in eq 4. The signal shown in orange dashed line in the m/e = 43 image and the m/e = 42 TOF spectrum were used to derive the net speed distribution (in the center of mass reference frame) of the detected vinoxy signal; this speed distribution is shown in Figure 12. In the Supporting

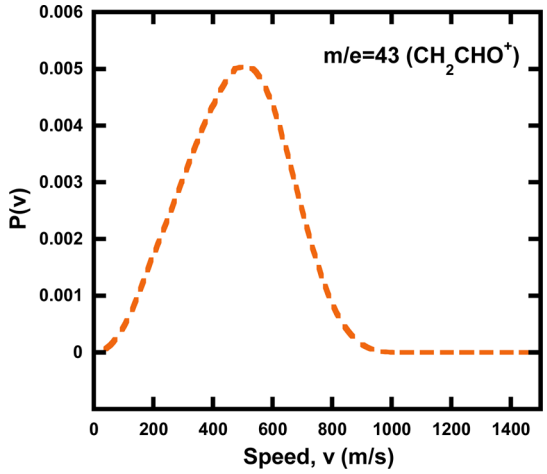

Figure 12. Speed distribution of the signal assigned to vinoxy product and normalized to unity. It was derived from fitting the signal shown by the dashed orange line in the m/e = 42 TOF spectrum (Figure 4) and the signal in the slow component that was not multiphoton in Figure 11.

Information and in the following paragraph we consider the possibility that this vinoxy signal comes from the dissociation of the high internal energy radicals to HBr + vinoxy; we conclude that it does not. Thus we show in Figure 12 only the measured net speed distribution of the vinoxy product that gave the orange line contribution to the signals in Figures 4, 10, and 11. The m/e = 43 photoionization signal is puny and compromised by multiphoton signal, but we also detected a much larger signal at m/e = 15, CH_3^+, from the dissociative photoionization of vinoxy radicals. Those data are shown in Figure 13. This is in

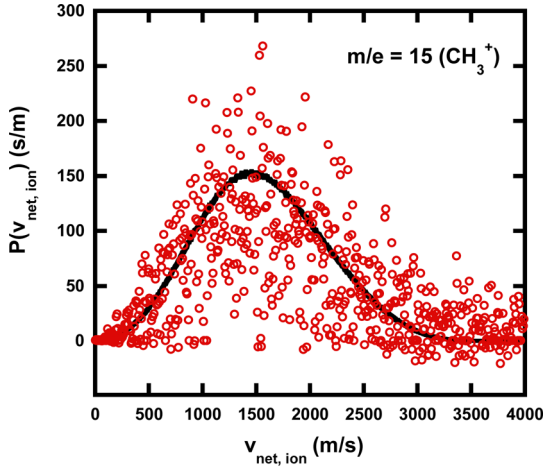

Figure 13. Distribution of net speeds of the signal at m/e = 15 (CH_3^+), derived from the image shown in the Supporting Information, using a photoionization energy of 10.55 eV. In fitting this signal, we added the additional recoil velocity imparted to the CH_3^+ ion fragment as the vinoxy radicals dissociatively ionize. This third velocity component was varied to fit the data; the corresponding $P(E_T)$ is shown in the Supporting Information. This third velocity component was added to the net speeds of the dissociatively ionizing vinoxy radicals shown by the orange dashed line in Figure 12 with an isotropic angular distribution to calculate the black line fit here.

dx.doi.org/10.1021/jp4095886 | J. Phys. Chem. A 2014, 118, 404−416

agreement with the prior reports of vinoxy radicals undergoing dissociative photoionization to m/e = 15. Unfortunately, the net speed of this m/e = 15 signal is altered from that of neutral vinoxy product from the dissociative photoionization. The fit shown in Figure 13 assumes that the dissociative photoionization of vinoxy radicals imparts additional recoil kinetic energy to the resulting CH_3^+ cations (given in the Supporting Information).

We now turn to whether we can identify the momentum-matched cofragment to the vinoxy product observed. If the high internal energy $BrCH_2CH_2O$ radicals dissociate to HBr + vinoxy, we may predict from the $P(E_{T,2^\circ})$ given in the Supporting Information (and an isotropic angular distribution between the primary and secondary velocity vectors) what the net speeds imparted to the HBr cofragment would be. The predicted signals are shown in the m/e = 82 ($H^{81}Br^+$) TOF spectrum in Figure 9 in the black dashed-line fit. This spectrum shows the signal at m/e = 82 from all sources is very small; it was accumulated for 22.4 million laser shots. It can have many overlapping contributions, so the fits are shown only to indicate where the predicted signals would lie. The only clear contribution to this spectrum is the dissociative ionization of stable $BrCH_2CH_2O$ radicals to HBr^+, though there is some additional underlying signal peaking near 290 μs that has the right arrival times to be the HBr momentum-matched to vinoxy. In the next paragraph we shown this signal at HBr^+ is a factor of 80 too small and so does not support the assignment of the vinoxy signal to the reaction in eq 4. The m/e = 82 TOF spectrum also confirms that O−NO photofission is the predominant photodissociation channel. The electron bombardment cross section of HBr is large, so if there had been even a 5% branching to HBr photoelimination to form HBr + $H_2CCHONO$ it would have appeared as an observable peak in this spectrum. Similarly, the TOF spectra at Br^+ and HBr^+ are very similar, so there is no apparent contribution from C−Br photofission; O−NO photofission dominates.

We now turn to examining whether the observed vinoxy signal could result from the reaction in eq 4, the dissociation of the $BrCH_2CH_2O$ radical to vinoxy + HBr. The signal at HBr^+ shown in Figure 9 was very low despite the fact that HBr has a larger electron bombardment ionization cross section than vinoxy. One can predict the ratio of signals we would see from each in the m/e = 42 and m/e = 82 TOF data on the basis of the fits presented above, in which dissociative ionization of vinoxy radicals completely accounts for the underlying signal in the TOF spectrum of m/e = 42, using the following expression:

$$\left(\frac{\text{signal at } m/e = 42 \text{ from vinoxy}}{\text{signal at } m/e = 82 \text{ from HBr}}\right)_{\text{predicted}} = \frac{\Phi_{\text{vinoxy}}}{\Phi_{\text{HBr}}}\left(\frac{\text{correction for vinoxy}}{\text{correction for HBr}}\right)\left(\frac{\sigma_{\text{ion,tot,vinoxy}}}{\sigma_{\text{ion,tot,HBr}}}\right)\left(\frac{\frac{f^{42}}{\text{vinoxy}}}{\frac{f^{82}}{\text{HBr}}}\right) \quad (5)$$

The values of Φ are the respective quantum yields of vinoxy radical and HBr. As stated above, by ruling out primary HBr photoelimination, the remaining most likely source of vinoxy, suggested by Miller and co-workers, is the reaction in eq 4 where the $BrCH_2CH_2O$ radicals dissociate to vinoxy + HBr. In this reaction, the ratio of their quantum yields, $\Phi_{\text{vinoxy}}/\Phi_{\text{HBr}}$, must be 1:1, so we can make a prediction for the relative strength of the two resulting signals. To do this, we must account for the respective total electron bombardment ionization cross section of vinoxy radical $\sigma_{\text{ion,tot,vinoxy}}$ and that of HBr, $\sigma_{\text{ion,tot,HBr}}$. The ratio $(f^{42}/\text{vinoxy})/(f^{82}/\text{HBr})$ accounts for the fractions of the detected ion mass, 42 and 82 amu, respectively, in the electron impact mass spectra of each. We must also include the usual correction for kinematic factors such as the Jacobian factors inherent in the signal in the TOF spectra and the different sensitivity to each product due to transit time in the electron bombardment ionizer. This is accounted for in the "correction for vinoxy" and the "correction for HBr". To get that ratio, we calculate a hypothetical TOF spectrum by executing a vector sum of the velocities of the radicals that could dissociate to HBr + vinoxy and the secondary recoil kinetic energy imparted to each that would give a net speed distribution consistent with that shown in orange dashed line for vinoxy in Figures 4, 10, and 11. But we do not scale the fits to match the measured spectra; we instead predict the relative integrated signals from vinoxy and from HBr that would be observed in the TOF spectra if they are produced in the required 1:1 ratio. (The program does not account for different ionization cross sections, or dissociative ionization upon electron impact so those terms multiply these corrections.)

The $\sigma_{\text{ion,tot}}$ value represents the total electron bombardment ionization cross-section for each species; they are estimated using the empirical relation (good to ±20%) of Center and Mandl, substituting the sum of atomic polarizabilities for the molecular polarizability. The fraction f of cations at the detected mass is estimated from the literature mass spectrum of vinoxy radicals for m/e = 42.[27] (Note that the ratio of signals we attributed to vinoxy at m/e = 42 to that at m/e = 29 is smaller than one would expect from ref 27, but we used the mass fragmentation pattern in ref 27 to substitute into eq 5 as that paper includes the entire mass spectrum.) The value of f used for HBr is taken from the literature mass spectrum of HBr,[31] in which the ratio of Br^+ and HBr^+ is 39:100 and also includes the fact that the signal at m/e = 82 is detecting only $H^{81}Br$ products.

$$\left(\frac{\text{signal at } m/e = 42 \text{ from vinoxy}}{\text{signal at } m/e = 82 \text{ from HBr}}\right)_{\text{predicted}} = \frac{1}{1}\left(\frac{0.64}{1}\right)\left(\frac{72.5}{51.4}\right)\left(\frac{0.24}{0.72/2}\right) = 0.60 \quad (6)$$

We may compare this predicted ratio of signals above to the actual signals at m/e = 42 (based on the signal under the orange line fit in the m/e = 42 TOF) and the signal under the corresponding fit in the m/e = 82 TOF spectrum. Though we did not alternate taking spectra at each mass but, instead, took the entire m/e = 42 TOF spectrum in one long run and the m/e = 82 spectrum in two long runs, the m/e = 30 data taken on the same days as the m/e = 42 TOF and one of the m/e = 82 TOFs show that signal varied by less than factor of 2 for these two days and all other days in which we took m/e = 30 TOF spectra. We find that the experimentally observed ratio based on counts per laser shot is greater than that predicted in eq 6 by a factor of 80. In other words, we have observed far less signal at HBr^+ than one would expect if the vinoxy product were formed in a 1:1 ratio with HBr. Therefore, the vinoxy signal we detect is definitely not from the dissociation of the $BrCH_2CH_2O$ radicals to vinoxy + HBr.

dx.doi.org/10.1021/jp4095886 | J. Phys. Chem. A 2014, 118, 404−416

IV. DISCUSSION

This study focused on characterizing the primary photodissociation channels of $BrCH_2CH_2ONO$ at 351 nm and the subsequent unimolecular dissociation channels of the nascent $BrCH_2CH_2O$ radicals produced from the O−NO bond photofission. It was motivated by the results of Miller and co-workers, who detected signal from both formaldehyde, a product one expects if the primary photodissociation channel is O−NO fission to form $BrCH_2CH_2O$ radicals, and vinoxy, an unexpected product.

Our data show that O−NO photofission is indeed the dominant primary photodissociation channel; neither HBr photoelimination nor C−Br photofission are significant primary photodissociation channels. This is in agreement with the conclusions of Miller and co-workers and in accord with the known photochemistry of alkyl nitrites in the structured absorption band accessed at 351 and 355 nm. Though the presence of the Br substituent does not alter the primary photodissociation channels at these excitation wavelengths, it would be interesting to see if excitation at 193 nm gives a different result. One might expect C−Br photofission to compete with O−NO photofission at 193 nm, as alkyl bromides have an excited state that is repulsive in the C−Br bond at those higher energies. Thus, upon excitation to S_2, 2-bromoethylnitrite might be expected to behave as a bichromophore; we have just begun a study at 193 nm.

The O−NO photofission channel at 351/355 nm produces $BrCH_2CH_2O$ radicals. Although using LIF Miller and co-workers reported detecting the halogenated ethoxy radical only when the halogen substituent was fluorine, not bromine or chlorine, the stable radicals were clearly detected at several daughter ions in our study here (though not at parent ion); the signal was momentum-matched to the NO cophotofragments. Our measured kinetic energy distribution allows us to estimate the internal energy distribution in the nascent $BrCH_2CH_2O$ radicals (section IIIB). Some of the radicals undergo subsequent dissociation, and our study is in agreement with Miller and co-workers that a major dissociation channel of $BrCH_2CH_2O$ radicals is to $CH_2Br + H_2CO$. Miller and co-workers detected the formaldehyde product and this work, using tunable VUV photoionization in an imaging apparatus, definitively detected the CH_2Br coproduct.

Miller and co-workers also report strong spectroscopic evidence for a vinoxy radical product from the photodissociation of halogenated alkyl nitrites, including $BrCH_2CH_2ONO$. They attribute that signal to a competing channel in the dissociation of the nascent $BrCH_2CH_2O$ radicals, a channel that forms vinoxy + HBr. Figure 3 shows that the barrier to the $CH_2Br + H_2CO$ channel is the lowest one, at 16 kcal/mol, whereas the barrier to the vinoxy + HBr product channel is 30 kcal/mol, so even the radicals formed with a high enough internal energy to in principle dissociate to vinoxy + HBr would be statistically unlikely to do so. This is what led Miller and co-workers to suggest that a roaming mechanism might be influencing the dynamics of the $BrCH_2CH_2O \rightarrow$ vinoxy + HBr reaction. Our data in section IIIE do evidence vinoxy radicals from the photolysis of this sample (the spectroscopic experiment of Miller and co-workers definitively detect vinoxy), but our HBr^+ data show that there is most certainly not enough HBr^+ signal from HBr to assign the vinoxy to the $BrCH_2CH_2O \rightarrow$ vinoxy + HBr reaction. Miller and co-workers also considered, and rejected, the possibility that the vinoxy results from a competing HBr photoelimination channel in the precursor that would produce CH_2CHONO (that product would efficiently dissociate to vinoxy + NO, as shown in the calculations of Gindulyte et al.[32]). The present study concurs that vinoxy cannot be from this source, again because the signal at HBr^+ is far too small to form in a 1:1 (or larger) ratio with vinoxy. We are frankly at a loss to determine the source of vinoxy signal detected in these experiments.

Irrespective of its source, one important result in this work was the photoionization detection of vinoxy radicals. Encouraged by the ability of tunable VUV photoionization detection in our imaging apparatus to selectively detect CH_2Br product that had been buried under signal from other species when detected with electron bombardment ionization, we sought to detect vinoxy product in our imaging apparatus. There have only been two prior reports of the photoionization detection of vinoxy. Though the study on O + ethene by Lee et al.[29] assigned both a small signal at m/e = 43 detected with photoionization to vinoxy products, and a larger signal at m/e = 15 to dissociative photoionization of vinoxy radicals, Osborn and co-workers,[30] studying products of the O + propene reaction, reported no signal at m/e = 43 from vinoxy but substantial signal at m/e = 15, with an onset near 10.2 eV (and increasing to 10.6 eV) that they assign to the dissociative photoionization of vinoxy radicals. The latter paper also reports a computational study of the vinoxy cation that supports the assigned dissociation of the cation to CO + CH_3^+. Our results are in agreement with those studies; we detected only a very small signal at m/e = 43 using a photoionization energy of 10.55 eV, but substantial signal at m/e = 15 using a photoionization energy of 10.6 eV. The latter is most likely from the photoionization of vinoxy radical (there is no other source of methyl cations in this work), but unfortunately the data show that the dissociative ionization of vinoxy to CO + CH_3^+ imparts a significant additional recoil velocity to the methyl cation. Thus, if one needs a velocity distribution of the neutral species, one should not detect vinoxy with photoionization in an imaging apparatus as the signal at m/e = 43 is prohibitively small and the signal at m/e = 15 has a speed distribution that is markedly changed by the cation dissociation dynamics. Instead, one should use electron bombardment ionization with detection at m/e = 42 or 29, or photoionization detection in a scattering apparatus where the photoionization occurs after the neutral product has flown to the detector. The most unambiguous method for detecting vinoxy if one does not need a velocity distribution is most certainly LIF.

■ ASSOCIATED CONTENT

Supporting Information

The Supporting Information includes (A) a UV absorption spectrum of $BrCH_2CH_2ONO$ and CH_3ONO, (B) NO^+ images taken at several photoionization energies with 355 nm excitation and their comparison with the scattering data, comparison of the $P(E_T)$ derived from the 355 nm image and the $P(E_T)$ used to fit the m/e = 30 scattering data taken at 351 nm, and comparison of the speed distributions derived from the NO images at various ionization energies, (C) angular distributions of the NO^+ signal taken in the scattering apparatus, (D) CH_2Br^+ images and electronic structure results on the IEs and AE, (E) detail on the analysis of the potential HBr + vinoxy channel, (F) tertiary $P(E_T)$ used to fit the detected net speeds of CH_3^+ from the dissociative photoionization of vinoxy, and (G) $P(E_{T,2^\circ})$ used in section III.E to

dx.doi.org/10.1021/jp4095886 | J. Phys. Chem. A 2014, 118, 404−416

arrive at a Jacobian correction for the vinoxy and possible HBr co-fragment signals. This information is available free of charge via the Internet at http://pubs.acs.org

AUTHOR INFORMATION

Corresponding Author

*L. Butler: e-mail, l-butler@uchicago.edu; phone, 773-702-7206.

Notes

The authors declare no competing financial interest.

ACKNOWLEDGMENTS

This work was supported by the Chemical Sciences, Geosciences and Biosciences Division, Office of Basic Energy Sciences, Office of Science, U.S. Department of Energy, under Grants DE-FG02-92ER14305 (L.J.B.) and DE-FG02-01ER14172 (T.A.M.). The introduction of tunable VUV photoionization to our imaging experiments was supported by the National Science Foundation under grant number CHE-1152043 (L.J.B). We thank UChicago undergraduate Mary Hillegass and former Ph.D. student Carrie Womack for their work on developing the VUV photoionization source and Ryan Booth for his help in training L.W. on the apparatus and maintaining the lasers and scattering apparatus.

REFERENCES

(1) Wayne, R. P. In *Chemistry of Atmospheres*, 3rd ed.; Oxford University: Oxford, U.K., 2000.

(2) Dixon, R. N.; Rieley, H. State-selected Photodissociation Dynamics of HONO($\tilde{A}^1A''$): Characterization of the NO Fragment. *J. Chem. Phys.* **1989**, *91*, 2308−2320.

(3) Vasudev, R.; Zare, R. N.; Dixon, R. N. Dynamics of Photodissociation of HONO at 369 nm: Motional Anisotropy and Internal State Distribution of the OH Fragment. *Chem. Phys. Lett.* **1983**, *96*, 399−402.

(4) Vasudev, R.; Zare, R. N.; Dixon, R. N. State-Selected Photodissociation Dynamics: Complete Characterization of the OH fragment Ejected by the HONO $\tilde{A}$ State. *J. Chem. Phys.* **1984**, *80*, 4863−4878.

(5) Brühlmann, U.; Dubs, M.; Huber, J. R. Photodissociation of Methylnitrite: State Distributions, Recoil Velocity Distribution, and Alignment Effects of the NO($X^2\Pi$) Photofragment. *J. Chem. Phys.* **1987**, *86*, 1249−1257.

(6) Lahmani, F.; Lardeux, C.; Solgadi, D. Rotational and Electronic Anisotropy in NO $X^2\Pi$ from the Photodissociation of CH_3ONO. *Chem. Phys. Lett.* **1986**, *129*, 24−30.

(7) Schwartz-Lavi, D.; Bar, I.; Rosenwaks, S. Rotational Alignment and Non-Statistical Λ Doublet Population in NO following $(CH_3)_3CONO$ Photodissociation. *Chem. Phys. Lett.* **1986**, *128*, 123−126.

(8) Yin, H. M.; Sun, J. L.; Li, Y. M.; Han, K. L.; He, G. Z. Photodissociation Dynamics of the S_2 State of CH_3ONO: State Distributions and Alignment Effects of the NO ($X^2\Pi$) Photofragment. *J. Chem. Phys.* **2003**, *118*, 8248−8255.

(9) Winniczek, J. W.; Dubs, R. L.; Appling, J. R.; McKoy, V.; White, M. G. A Multiphoton Ionization Study of the Photodissociation Dynamics of the S_2 State of CH_3ONO. *J. Chem. Phys.* **1989**, *90*, 949−963.

(10) Benoist d'Azy, O.; Lahmani, F.; Lardeux, C.; Solgadi, D. State-Selective Photochemistry: Energy Distribution in the NO Fragment after Photodissociation of the CH_3ONO nπ^* State. *Chem. Phys.* **1985**, *94*, 247−256.

(11) Finke, H.; Spiecker, H.; Andreson, P. The Photodissociation of tert-Butyl Nitrite at 193 nm. *J. Chem. Phys.* **1999**, *110*, 4777−4782.

(12) Castle, K. J.; Abbott, J.; Peng, X.; Kong, W. Photodissociation of *t*-Butyl Nitrite Between 200 and 250 nm: Internal Energy Distribution of NO. *Chem. Phys. Lett.* **2000**, *318*, 565−570.

(13) Schwartz-Lavi, D.; Rosenwaks, S. Scalar and Vectorial Properties in the Photodissociation of tert-Butyl Nitrite from the S_1 and S_2 States. *J. Chem. Phys.* **1988**, *88*, 6922−6930.

(14) Hippler, M.; Al-Janabi, F. A. H.; Pfab, J. Photodissociation of Jet-Cooled Methyl and *t*-Butyl Nitrite near 380 nm. *Chem. Phys. Lett.* **1992**, *192*, 173−178.

(15) Chhantyal-Pun, R.; Chen, M.-W.; Sun, D.; Miller, T. A. Detection and Characterization of Products from Photodissociation of XCH_2CH_2ONO (X = F, Cl, Br, OH). *J. Phys. Chem. A* **2012**, *116*, 12032−12040.

(16) Nonella, M.; Huber, J. R. Photodissociation of Methynitrite: An MCSCF Calculation of the S_1 Potential Surface. *Chem. Phys. Lett.* **1986**, *131*, 376−379.

(17) Mestdagh, J. M.; Berdah, M.; Dimicoli, I.; Mons, M.; Meynadier, P.; d'Oliveira, P.; Piuzzi, F.; Visticot, J. P.; Jouvet, C.; Lardeux-Dedonder, C.; et al. Observation of an Indirect Pathway in the Femtosecond Study of Alkyl Nitrite Photodissociation in the S_1 State. *J. Chem. Phys.* **1995**, *103*, 1013−1023.

(18) Kades, E.; Rosslein, M.; Bruhlmann, U.; Huber, J. R. Photodissociation of Methyl Nitrite CH_3ONO, Butyl Nitrite $(CH_3)_3CONO$, and the Clusters $[CH_3ONO]_n$ and $[(CH_3)_3CONO]_n$. *J. Phys. Chem.* **1997**, *97*, 989−996.

(19) Castle, K. J.; Kon, W. Directions of Transition Dipole Moments of *t*-Butyl Nitrite Obtained via Orientation with a Strong, Uniform Electric Field. *J. Chem. Phys.* **2000**, *112*, 10156−10161.

(20) Parker, D. H; Eppink, A. T. J. B. Velocity Map Imaging of Ions and Electrons Using Electrostatic Lenses: Application in Photoelectron and Photofragment Ion Imaging of Molecular Oxygen. *Rev. Sci. Intrum* **1997**, *68*, 3477−3484.

(21) Chang, B.; Hoetzlein, R. C.; Mueller, J. A.; Geiser, J. D.; Houston, P. L. Improved Two-Dimensional Product Imaging: The Real-time Ion-Counting Method. *Rev. Sci. Instrum.* **1998**, *69*, 1665−1670.

(22) Chandler, D. W.; Houston, P. L. Two-Dimensional Imaging of State-Selected Photodissociation Products Detected by Multiphoton Ionization. *J. Chem. Phys.* **1987**, *87*, 1445−1447.

(23) Zhou, J.; Jones, B.; Yang, X.; Jackson, W. M.; Ng, C. Y. A Vacuum Ultraviolet Laser Photoionization and Pulsed Field Ionization Study of Nascent S($^3P_{2,1,0}$; $^1D_2$) Formed in the 193.3 nm Photodissociation of CS_2. *J. Chem. Phys.* **2008**, *128*, 014305.

(24) Barker, J. R. *MULTIWELL*; University of Michigan, Ann Arbor, MI, 2010.

(25) Tarte, P. Rotational Isomerism as a General Property of Alkyl Nitrites. *J. Chem. Phys.* **1952**, *20*, 1570−1575.

(26) Alligood, B. W.; Straus, D. B.; Butler, L. J. Analyzing Velocity Map Images to Distinguish the Primary Methyl Photofragments from Those Produced Upon C−Cl Bond Photofission in Chloroacetone at 193 nm. *J. Chem. Phys.* **2011**, *135*, 034302.

(27) Schmoltner, A. M.; Chu, P. M.; R. Brudzynski, R. J.; Lee, Y. T. Crossed Molecular Beam Study of the Reaction O(^3P) + C_2H_4. *J. Chem. Phys.* **1989**, *91*, 6926−6936.

(28) Morton, M. L.; Szpunar, D. E.; Butler, L. J. Photodissociating Methyl Vinyl Ether to Calibrate O + Ethylene Product Branching and to Test Propensity Rules for Product Channel Electronic Accessibility. *J. Chem. Phys.* **2001**, *115*, 204−216.

(29) Lee, S.-H.; Huang, W. J.; Chen, W. K. Dynamics of the Reaction of Atomic Oxygen with Ethene: Observation of All Carbon-Containing Products by Single-Photon Ionization. *Chem. Phys. Lett.* **2007**, *446*, 276−280.

(30) Savee, J. D.; Welz, O.; Taatjes, C. A.; Osborn, D. L. New Mechanistic Insights to the O(^3P) + Propene Reaction from Multiplexed Photoionization Mass Spectrometry. *Phys. Chem. Chem. Phys.* **2012**, *14*, 10410−10423.

(31) NIST Mass Spectrometry Data Center. http://webbook.nist.gov.

(32) Gindulyte, A.; Massa, L.; Huang, L.; Karle, J. Ab Initio Study of Unimolecular Decomposition of Nitroethylene. *J. Phys. Chem. A* **1999**, *103*, 11040−11044.